Int. J. Heat Mass Transfer. Vol. 36, No. 10, pp. 2499–2509, 1993
Printed in Great Britain

0017–9310/93 $6.00 + 0.00

Melting around a shaft rotating in a phase-change material

AL. M. MOREGA, A. M. FILIP and A. BEJAN
Department of Mechanical Engineering and Materials Science, Duke University, Box 90300, Durham, NC 27708-0300, U.S.A.

and

P. A. TYVAND
Department of Agricultural Engineering, Agricultural University of Norway, P.O. Box 5065, N-1432 Ås, Norway

(*Received* 21 *October* 1992 *and in final form* 30 *December* 1992)

Abstract—In this paper we describe the thin-film melting of a block of solid phase-change material (the bearing) around a rotating cylinder (the shaft). We determine the relation between the force applied on the shaft and the speed with which the shaft migrates into the bearing, the relation between the applied force and the torque, and the angle between the applied force and the direction of migration into the bearing. The method is based on contact melting theory, which combines the Reynolds thin-film lubrication theory with an analysis of phase-change heat transfer in the melt. The paper addresses three limiting regimes of the contact melting phenomenon: (1) the long bearing with melting due to frictional heating in the melt layer; (2) the short bearing with melting due to frictional heating in the melt layer, and (3) the short bearing with melting due to a temperature difference imposed between the hot cylinder and the cold phase-change material.

1. INTRODUCTION

THE MELTING phenomenon described in this paper is recommended by an important consideration in the design and operation of journal bearings. Frictional heat generation and the differential thermal expansion properties of the shaft and the bushing may lead to complete loss of clearance and seizure. The time-dependent heat conduction and thermoelastic processes that lead to the disappearance of the clearance were described most recently by Bishop and Ettles [1], Dufrane and Kannel [2], and Khonsari and Kim [3]. In this paper we focus on what can happen *after* the complete loss of clearance, if the bushing melts due to frictional heat generation, and seizure is prevented. The melt lubrication effect can be an essential safety feature in the design of machines where accidental bearing seizure cannot be tolerated.

The problem of melting and thin-film lubrication around a shaft embedded in a melting solid can be studied based on the method of contact melting theory. This method was developed during the last decade, beginning with studies of contact melting inside capsules containing phase-change materials for energy storage [4–13]. Contact melting analyses were also developed for predicting the speed with which a hot object sinks by melting into a solid block of phase-change material [14–17]. The lubrication characteristics of a plane surface that melts because of an imposed temperature difference, or because of friction, were also described analytically [18–21]. Experimental studies [18, 21–23] and numerical simulations [24, 25] have validated the predictions made based on contact melting theory.

In view of the progress made on contact melting, in this paper we proceed analytically and numerically to describe the melting around the rotating shaft in three limiting regimes. In the first part we consider the case where the bearing is longer than the shaft radius, and the melting is caused entirely by the viscous heating of the melt layer. In the second part we solve the corresponding frictional melting problem for a bearing that is shorter than the shaft radius. Finally, in the third part we analyze the melting caused by a temperature difference that is maintained between the shaft and the surrounding solid phase-change material.

2. THE LONG BEARING ($B \gg R$): MELTING DUE TO VISCOUS DISSIPATION

We begin with the analysis of the melting and erosion due to viscous heating in the liquid film when the bearing material is at the melting point, and the shaft does not provide an escape route for the heat generated in the liquid film. Two limiting bearing geometries are of interest. In this section we consider the relatively long bearing, that is, one in which the axial contact length B is considerably larger than the shaft radius R. This limiting geometry is illustrated in Fig.

NOMENCLATURE

A_C, A_I acceleration factors, equation (40)
B axial length of contact, Fig. 8
C constant of integration, equation (17)
f dimensionless applied force, equation (22)
$\bar{f}$ dimensionless applied force, $\bar{F}/\rho h_{sf} R$
F force per unit axial length, Fig. 1
F_B total force, Fig. 8
$\bar{F}$ average force, F_B/B
G negative of the pressure gradient, equation (6)
$\tilde{G}$ dimensionless pressure gradient, equation (15)
h_{sf} latent heat of melting
$I_a, \ldots, I_r$ integrals, equations (30)–(33)
k thermal conductivity of liquid
N order of Gauss quadrature, equation (23)
P pressure
$\tilde{P}$ dimensionless pressure, equation (15)
R radius
T_m melting point
T_s shaft temperature
$\tilde{T}_s$ dimensionless shaft temperature, equation (42)
$\hat{u}, \hat{v}$ velocity components
U peripheral speed, ωR
V shaft translational speed, Fig. 1
$\tilde{V}$ dimensionless shaft translational speed, equation (16)
w_i weight associated with x_i, equation (23)
W_C, W_I weights, equation (40)
$\hat{x}, \hat{y}$ curvilinear coordinates, Fig. 1
x_i roots of Legendre polynomials
Y inverse of the film thickness, $1/\tilde{\delta}$
z axial coordinate, Fig. 8.

Greek symbols
β peripheral coordinate, Fig. 1
δ film thickness
$\bar{\delta}$ average film thickness
$\tilde{\delta}$ dimensionless film thickness, equation (16)
$\varepsilon_I, \varepsilon_C, \varepsilon_\theta$ relative errors, equations (37)
θ angular coordinate
θ_0 angle, Fig. 1
μ viscosity
ρ density
τ wall shear stress, equation (14)
$\tilde{\tau}$ dimensionless wall shear stress, equation (15)
φ angular coordinate
ω angular speed
$\omega(x)$ integrable kernel
Ω dimensionless angular speed, equation (22).

Subscript
$(\ )_{avg}$ average.

1, which shows that the liquid film is two-dimensional (in the plane perpendicular to the shaft axis). The opposite limit in which the bearing is relatively short ($B \ll R$), and where the liquid flows in the axial direction forms the subject of Sections 5 and 6.

In Fig. 1 the y-direction is defined by the direction of the relative translational motion between the shaft and the surrounding solid bearing: seen from our frame of reference there is a uniform upward flow V of solid material, which melts and flows around the cylinder as a very thin film for $y < 0$. For $y > 0$ there is a much wider wake of earlier melted bearing material: the flow in this wake is not affected by the flow in the thin film. For $y > R$ we assume that the wake will have an almost uniform velocity V and be at hydrostatic pressure.

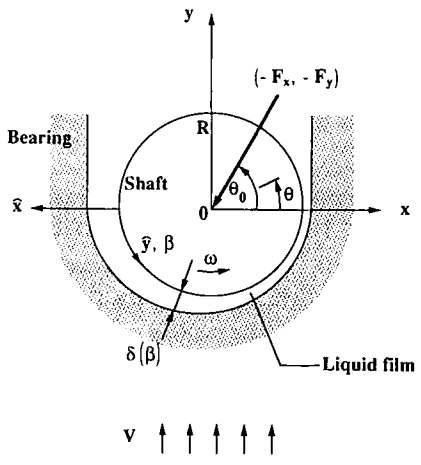

FIG. 1. Cross-section through a long bearing that melts due to the heating caused by viscous dissipation in the film.

The film thickness δ is a function of the angle θ, where (r, θ) are polar coordinates, and $\bar{\delta}$ denotes the film thickness averaged from $\theta = \pi$ to $\theta = 2\pi$. The cylindrical shaft rotates with an angular velocity ω, which means that the peripheral velocity of the cylinder is $U = \omega R$. The translational velocity between the shaft and the solid bearing is assumed very small compared with this peripheral velocity, $V \ll U$.

Our thin-film analysis will then be carried out to the leading order of the two small parameters $\bar{\delta}/R$ and V/U. The translational velocity V is a result of the external force per unit axial length $-\mathbf{F} = (-F_x, -F_y)$ applied on the cylinder. However, we choose not to pose the problem with $|\mathbf{F}|$ given: we assume that V is given *a priori*, and will find $\mathbf{F}$ as a result of compu-

tation. This has the advantage that we can solve the hydrodynamic problem without knowing the tilting angle θ_0 defined by:

$$\theta_0 = \arctan(F_y/F_x). \tag{1}$$

This angle will instead be determined *a posteriori*. With our choice of posing the problem, we can regard V/U as our primary small parameter, so that the other small parameter δ/R will be derived from it.

For the thin-film analysis it is convenient to introduce a local curvilinear coordinate system $(\hat{x}, \hat{y})$ along the cylinder contour:

$$\hat{x} = r - R, \quad \hat{y} = R(\theta - \varphi). \tag{2}$$

Here φ is a fixed, arbitrary angle. The Jacobian of this transformation can be written:

$$\frac{\partial(x, y)}{\partial(\hat{x}, \hat{y})} = 1 + \frac{\hat{x}}{R} = 1 + O\left(\frac{\delta}{R}\right) \tag{3}$$

when we consider the thin film where $0 < \hat{x} < \delta$. Equation (3) shows that it is possible to treat the curvilinear coordinate system $(\hat{x}, \hat{y})$ as if it were an orthogonal coordinate system with no local curvature and constant metric, but only as long as we work exclusively to the leading order in our thin-film expansion. From now on we choose $\varphi = \pi$, so that the new angular coordinate is $\beta = \theta - \pi = \hat{y}/R$.

The thin-film approximation for small Reynolds number flow is:

$$\nabla P = \mu \frac{\partial^2 \mathbf{V}}{\partial \hat{x}^2} \tag{4}$$

where P is the pressure and μ the dynamic viscosity of the melted bearing. Let us decompose the liquid velocity vector $\mathbf{V}$ into its components $\hat{u}$ and $\hat{v}$ along the $\hat{x}$ and $\hat{y}$ axes. To the leading order in the small parameter V/U, the boundary conditions for the local Couette–Poiseuille flow will be:

$$\begin{aligned} &\hat{v} = U \quad \text{at} \quad \hat{x} = 0 \\ &\hat{v} = 0 \quad \text{at} \quad \hat{x} = \delta(\hat{y}). \end{aligned} \tag{5}$$

In terms of the negative of the pressure gradient

$$G(\hat{y}) = -\frac{dP}{d\hat{y}} \tag{6}$$

the thin-film Couette–Poiseuille flow is given by

$$\hat{v}(\hat{x}, \hat{y}) = \frac{G(\hat{y})}{2\mu}(\delta - \hat{x})\hat{x} + U\left(1 - \frac{\hat{x}}{\delta}\right) \tag{7}$$

where $\delta = \delta(\hat{y})$ is still an unknown function, and the thin-film approximation implies that it is slowly varying compared with the average thickness δ.

The continuity equation for a thin incompressible fluid film requires:

$$\frac{\partial \hat{u}}{\partial \hat{x}} = -\frac{\partial \hat{v}}{\partial \hat{y}} = -\frac{G'}{2\mu}(\delta - \hat{x})\hat{x} - \frac{G\delta'\hat{x}}{2\mu} - U\frac{\delta'\hat{x}}{\delta^2} \tag{8}$$

where the primes denote derivatives with respect to $\hat{y}$.

The boundary conditions for the radial flow component are

$$\begin{aligned} &\hat{u} = 0 \quad \text{at} \quad \hat{x} = 0 \\ &\hat{u} = -V\sin\beta \quad \text{at} \quad \hat{x} = \delta. \end{aligned} \tag{9}$$

To work consistently to the leading order in the thin-film approximation implies that the effect of varying film thickness is disregarded in the second boundary condition. We integrate equation (8) with respect to $\hat{x}$, and apply the boundary conditions (9):

$$\delta^3 G' + 3\delta^2\delta' G + 6\mu U\delta' = 12\mu V\sin\beta. \tag{10}$$

A second coupled nonlinear equation for the film thickness and the pressure gradient is the energy balance equation:

$$\frac{\delta^3}{12\mu}G^2 + \mu\frac{U^2}{\delta} = \rho h_{sf} V\sin\beta. \tag{11}$$

The left side of equation (11) was obtained by integrating the volumetric heat generation rate $\mu(\partial\hat{v}/\partial\hat{x})^2$ across the liquid film. Equation (11) states that all the mechanical energy that is dissipated in the Couette–Poiseuille flow is converted into latent heat at the melting front of the bearing. It is assumed throughout this study that the Peclet number $U\delta/\alpha$ is smaller than 1, so that convection in the β direction is negligible relative to radial conduction.

The problem statement concludes with the vertical and horizontal force balances for the shaft,

$$F\sin\theta_0 = \int_0^\pi (P\sin\beta - \tau\cos\beta)R\,d\beta \tag{12}$$

$$F\cos\theta_0 = \int_0^\pi (P\cos\beta + \tau\sin\beta)R\,d\beta \tag{13}$$

where $F = (F_x^2 + F_y^2)^{1/2}$, and τ is the shear stress on the shaft surface,

$$\tau = \tfrac{1}{2}G\delta - \mu\frac{U}{\delta}. \tag{14}$$

It is convenient to nondimensionalize equations (10)–(14) by introducing the variables

$$\tilde{P} = \frac{P}{F/R}, \quad \tilde{G} = \frac{G}{F/R^2}, \quad \tilde{\tau} = \frac{\tau}{F/R} \tag{15}$$

$$\tilde{\delta} = \delta\left(\frac{\rho h_{sf}}{\mu U R}\right)^{1/2}, \quad \tilde{V} = V\frac{R}{U}\left(\frac{\rho h_{sf}}{\mu U R}\right)^{1/2}. \tag{16}$$

The resulting nondimensional governing equations for the β domain 0–π are, in order,

$$f\tilde{\delta}^3\tilde{G} + 6\tilde{\delta} = C - 12\tilde{V}\cos\beta \tag{17}$$

$$f^2\tilde{\delta}^3\tilde{G}^2 + \frac{12}{\tilde{\delta}} = 12\tilde{V}\sin\beta \tag{18}$$

$$\sin\theta_0 = \int_0^\pi (\tilde{P}\sin\beta - \tilde{\tau}\cos\beta)\,d\beta \tag{19}$$

$$\cos\theta_0 = \int_0^\pi (\tilde{P}\cos\beta + \tilde{\tau}\sin\beta)\,d\beta \tag{20}$$

$$\tilde{\tau} = \tfrac{1}{2}\Omega^{1/2}\tilde{\delta}\tilde{G} - \frac{\Omega^{1/2}}{f\tilde{\delta}} \tag{21}$$

where f is the nondimensional applied force, and Ω is the nondimensional angular speed,

$$f = \frac{F}{\rho h_{sf} R}, \quad \Omega = \frac{\mu\omega}{\rho h_{sf}}. \tag{22}$$

Note that the momentum equation (17) was obtained by integrating equation (10) once in β, and that C is the integration constant. The pressure boundary conditions are $\tilde{P} = 0$ at $\beta = 0$ and $\beta = \pi$. The same conditions were used in previous analyses of contact melting around hot embedded solids [14, 15].

3. NUMERICAL METHOD

The problem formulated in equations (6) and (17)–(21) consists of finding the unknown functions $\tilde{\delta}(\beta)$, $\tilde{G}(\beta)$ and $\tilde{P}(\beta)$, and the unknown constants C, $\tilde{V}$ and θ_0, when the external parameters f and Ω are given. This problem belongs to functional analysis, as the solution to the nonlinear algebraic system (17), (18) is represented by the functions $\tilde{G}(\beta)$ and $\tilde{\delta}(\beta)$. The development of a solution method is far from straightforward because of the following features:

(a) Equations (19) and (20) are of the integral type, and there is no *a priori* information regarding their integrands (specifically, the behavior of $\tilde{G}$ and $\tilde{\delta}$).

(b) There is a lack of information regarding the smoothness of the functions $\tilde{G}(\beta)$ and $\tilde{\delta}(\beta)$, and their behavior in the limits $\beta \to 0$ and $\beta \to \pi$. From the geometry of Fig. 1 it is known that $\tilde{\delta}(\beta)$ is a strictly positive-definite quantity, but nothing can be said about its smoothness. The pressure gradient function $\tilde{G}(\beta)$ is of a lower smoothness class than the pressure function $\tilde{P}(\beta)$. We expect the $\tilde{G}(\beta)$ function (i) to change sign in order to satisfy the pressure boundary conditions $\tilde{P}(0) = \tilde{P}(\pi) = 0$, and (ii) to be at least a uniform-continuous function, in order not to induce discontinuities in $\tilde{P}(\beta)$. Because of this lack of information it is not advantageous to formulate the solution algorithm in terms of $\tilde{G}(\beta)$.

(c) Equation (18) shows that in the limits $\beta \to 0$ and $\beta \to \pi$ the right-hand side vanishes, while $\tilde{\delta} \to \infty$ and $\tilde{\delta}^3\tilde{G}^2 \to 0$. This means that in the same limits $\tilde{G}$ approaches zero and $\tilde{\delta}$ approaches infinity in such a way that $\tilde{\delta}^3\tilde{G}^2 \to 0$. These conclusions can be used only to check the solution *a posteriori*, and to justify the use of $Y = 1/\tilde{\delta}$ instead of $\tilde{\delta}$ in the selected method, in order to avoid the numerical difficulties associated with evaluating the integrals (19) and (20).

(d) There is no information on the behavior of the kernels of integrals (19) and (20), except that they should produce convergent integrals.

(e) The most we can say at this point about the constant $\tilde{V}$ is that it must be positive.

(f) The constant C is ill-defined numerically. Equation (17) implies that in the limits $\beta \to 0$ and $\beta \to \pi$ the left-hand side, LHS $= f\tilde{\delta}^3\tilde{G} + 6\tilde{\delta}$, must be finite. As shown at (c), however, in these limits the finite LHS would have to be calculated as the difference between two infinitely large terms—numerically, a very difficult task. At this stage we cannot anticipate either the sign or the range of C.

We selected the solution method by reasoning that sooner or later numerical integration techniques have to be used to deal with equations (19) and (20). We chose the Gauss quadrature, which for the order N is defined as

$$\int_a^b F(x)\,dx = \int_a^b f(x)\omega(x)\,dx \cong \sum_{i=1}^{N} f(x_i)w_i \tag{23}$$

where $\omega(x)$ is the integrable kernel. For Gauss–Legendre quadrature we substitute $\omega(x) = 1$, $a = -1$, $b = 1$; x_i are the roots of the Legendre polynomial of order N, and w_i are the associated weights. The Gauss–Legendre quadrature rule of order N, $\{w_i, x_i\}_{i=1}^N$, is available in tabulated form [26, 27]. This quadrature can be used if we assume that the integrands (19) and (20) are smooth enough (at least nonsingular) throughout the domain $0 \leqslant \beta \leqslant \pi$. In brief, the method we used is a collocation extension of the Gauss–Legendre quadrature, which allows us to bracket iteratively the values of $\tilde{V}$ and C, by using several orders for the Gauss–Legendre rule ($N = 13, 14, \ldots, 30$).

The integral equations (19, 20) were first written in terms of $\tilde{G}$, instead of $\tilde{P}$, by integrating by parts and using $\tilde{P} = 0$ at $\beta = 0, \pi$:

$$\sin\theta_0 = -\int_0^\pi (\tilde{G} + \tilde{\tau})\cos\beta\,d\beta \tag{24}$$

$$\cos\theta_0 = \int_0^\pi (\tilde{G} + \tilde{\tau})\sin\beta\,d\beta. \tag{25}$$

The momentum equation (17) and the shear stress formula (21) were then written in terms of the inverse of the film thickness $Y = 1/\tilde{\delta}$,

$$\tilde{G}(\beta) = \frac{Y^2}{f}[Y(C - 12\tilde{V}\cos\beta) - 6] \tag{26}$$

$$\tilde{\tau}(\beta) = \frac{\Omega^{1/2}}{f} Y\left[\frac{Y}{2}(C - 12\tilde{V}\cos\beta) - 4\right]. \tag{27}$$

By substituting equations (26) and (27) into the integrals (24) and (25) we obtain

$$\cos\theta_0 = 12\tilde{V}I_a + CI_b + I_c \tag{28}$$

$$-\sin\theta_0 = 12\tilde{V}I_d + CI_e + I_f \tag{29}$$

where the six coefficients of type I are unknown definite integrals:

$$I_a = -\frac{1}{f}\int_0^\pi Y^2\left(Y+\frac{\Omega^{1/2}}{2}\right)\cos\beta\sin\beta\,d\beta \quad (30a)$$

$$I_b = \frac{1}{f}\int_0^\pi Y^2\left(Y+\frac{\Omega^{1/2}}{2}\right)\sin\beta\,d\beta \quad (30b)$$

$$I_c = -\frac{6}{f}\int_0^\pi Y\left(Y+\frac{\Omega^{1/2}}{2}\right)\sin\beta\,d\beta - \frac{\Omega^{1/2}}{f}\int_0^\pi Y\sin\beta\,d\beta \quad (30c)$$

$$I_d = -\frac{1}{f}\int_0^\pi Y^2\left(Y+\frac{\Omega^{1/2}}{2}\right)\cos^2\beta\,d\beta \quad (30d)$$

$$I_e = \frac{1}{f}\int_0^\pi Y^2\left(Y+\frac{\Omega^{1/2}}{2}\right)\cos\beta\,d\beta \quad (30e)$$

$$I_f = -\frac{6}{f}\int_0^\pi Y\left(Y+\frac{\Omega^{1/2}}{2}\right)\cos\beta\,d\beta - \frac{\Omega^{1/2}}{f}\int_0^\pi Y\cos\beta\,d\beta. \quad (30f)$$

Equations (28, 29) and the identity $\sin^2\theta_0+\cos^2\theta_0 = 1$ produce a second order equation in $\tilde{V}$,

$$(12\tilde{V}I_a+I_r)^2+(12\tilde{V}I_d+I_s)^2 = 1 \quad (31)$$

where $I_r = CI_b+I_c$, and $I_s = CI_e+I_f$. Only the positive root $\tilde{V}$ of equation (31) is of interest.

Another relation between $\tilde{V}$ and C is obtained by integrating the $\tilde{G}$ expression (26) from $\beta = 0$ to $\beta = \pi$, and noting that the value of the $\tilde{G}$ integral must be zero because $\tilde{P}(0) = \tilde{P}(\pi)$,

$$C = \frac{I_o+12\tilde{V}I_n}{I_m} \quad (32)$$

where

$$I_m = \int_0^\pi Y^3\,d\beta, \quad I_n = \int_0^\pi Y^3\cos\beta\,d\beta,$$

$$I_o = 6\int_0^\pi Y^2\,d\beta. \quad (33)$$

By eliminating $\tilde{G}$ between the original momentum and energy equations (17), (18) we obtain the third order functional equation in $Y(\beta)$ with real coefficients,

$$Y^3(C-12\tilde{V}\cos\beta)^2-12Y^2(C-12\tilde{V}\cos\beta)+48Y-12\tilde{V}\sin\beta = 0 \quad (34)$$

which has at least one real root. Worth noting is that the root $Y = \tilde{V}\sin\beta$ is also obtained during the derivation of equation (34): this root is not acceptable because it does not satisfy equation (18). The final element necessary for constructing the algorithm is the pressure distribution, i.e. the integral of equation (26)

$$\tilde{P}(\beta) = \tilde{P}(0)-\int_0^\beta \tilde{G}(\beta)\,d\beta. \quad (35)$$

The numerical algorithm consisted of the following steps:

(1) Assume starting values for $\tilde{V}$ and C.

(2) Use the collocation technique to solve equation (34) for the known β_i $(i = 1,2,\ldots,N)$ roots of the Gauss–Legendre rule of order $N = 13,\ldots,30$.

(3) Use the Y_i solutions and the same quadrature to estimate the definite integrals labeled I.

(4) Compute the new melting speed value, $\tilde{V}_{new}$, by using equation (31).

(5) Compute the new value C_{new} using equation (32) and $\tilde{V}_{new}$.

(6) Compute the two θ_0 values furnished by equations (28) and (29)

$$\theta_0^{cos} = \cos^{-1}(12\tilde{V}_{new}I_a+C_{new}I_b+I_c)$$
$$\theta_0^{sin} = -\sin^{-1}(12\tilde{V}_{new}I_d+C_{new}I_e+I_f). \quad (36)$$

(7) Compute the relative iteration errors

$$\varepsilon_V = 1-\frac{\tilde{V}}{\tilde{V}_{new}}, \quad \varepsilon_C = 1-\frac{C}{C_{new}}$$
$$\varepsilon_\theta = 1-(\sin^2\theta_0+\cos^2\theta_0) \quad (37)$$

where $\sin\theta_0$ is given by equation (28), and $\cos\theta_0$ is given by equation (29).

(8) Stop if $\varepsilon_V < 10^{-6}$, $\varepsilon_C < 10^{-6}$ and $\varepsilon_\theta < 10^{-5}$; if not, update $\tilde{V}$ and C, and repeat the sequence. These error limits led to θ_0^{cos} and θ_0^{sin} values that had the same first five significant digits.

After the iterative scheme converged, we performed an additional accuracy test by setting $\tilde{P}(0) = 0$ and calculating $\tilde{P}(\pi)$ using equation (35). This calculation was based also on the Gauss–Legendre quadrature using an adaptive trial-and-error algorithm for $N = 6$ and $N = 17$. An initial integration step of length $\pi/100$ was assumed and, if necessary, reduced so that the relative local error produced by the two quadratures was less than 10^{-4}. The error

$$\varepsilon_P = \frac{\tilde{P}(\pi)}{\tilde{P}_{max}-\tilde{P}_{min}} \quad (38)$$

measured the degree to which successive calculations of the $\tilde{P}(\beta)$ curve satisfied $\tilde{P}(\pi) = 0$, as the order N was varied from 13 to 30. In the denominator of equation (38), $\tilde{P}_{max}$ and $\tilde{P}_{min}$ are, respectively, max $(\tilde{P})$ and min $(\tilde{P})$ in the β domain $[0,\pi]$. In this way we were able to bracket the sought $\tilde{V}$ and C values (i.e. to calculate the two 'best' estimates $(\tilde{V}_1,\tilde{V}_2)$ and (C_1,C_2)) so that ε_P did not exceed 5%. We then compared the ε_P values produced by the arithmetic mean of these brackets, and calculated the final values for $\tilde{V}$ and C by using the first-order (gradient) corrections

$$\tilde{V} = \tfrac{1}{2}(\tilde{V}_1+\tilde{V}_2)-\tfrac{1}{2}(\varepsilon_{P,1}+\varepsilon_{P,2})\frac{\tilde{V}_2-\tilde{V}_1}{\varepsilon_{P,1}-\varepsilon_{P,2}}$$

$$C = \tfrac{1}{2}(C_1 + C_2) - \tfrac{1}{2}(\varepsilon_{P,1} + \varepsilon_{P,2}) \frac{C_1 - C_2}{\varepsilon_{P,1} - \varepsilon_{P,2}}. \quad (39)$$

This choice of $\tilde{V}$ and C led consistently to ε_P values less than 0.1%.

Several critical aspects of the implementation of the iterative scheme are worth mentioning. To keep the convergence in $\tilde{V}$ and C under control we had to use an adaptive rule for calculating the restart values,

$$\tilde{V} = \frac{W_V \tilde{V} + A_V \tilde{V}_{\text{new}}}{W_V + A_V}, \quad C = \frac{W_C C + A_C C_{\text{new}}}{W_C + A_C} \quad (40)$$

where the acceleration factors A_V and A_C had values in the range 0–5. The weights are

$$W_{(V,C)} = \max\{W_{(V,C),\max} - [|\ln \varepsilon_{(V,C)}|], 0\},$$

where $W_{(V,C),\max}$ are the prescribed limits, and where the square brackets mean 'the integer part of.' The weights were given different values (typically, $W_V > W_C$) because the guesses for $\tilde{V}$ and C covered different intervals, namely, smaller for $\tilde{V}$ (only positive), and larger for C (positive and negative). The initial guess for $\tilde{V}$ and C was based either on the solutions obtained already for other quadrature rules (other N's) when f and Ω were fixed, or on the solution for a neighboring (f, Ω) case when the order N was fixed. The number of iterations ranged from 30 to 400.

A Newton Raphson/secant combination was used for solving equation (34). The entire scheme was implemented and run under MATHEMATICA®. The roots and weights for the Gauss–Legendre quadrature were obtained using a code based on the procedure developed by Golub and Welsch [26].

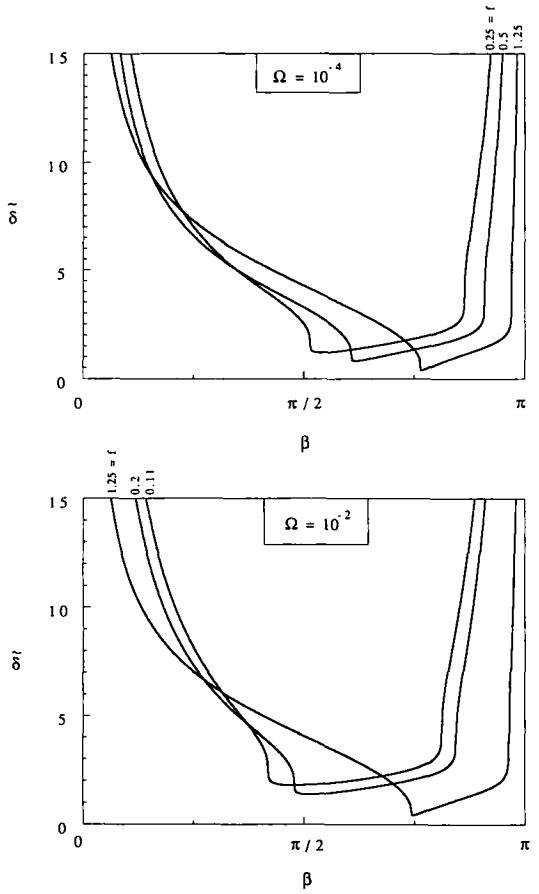

FIG. 2. The thickness of the liquid film caused by frictional melting in a long bearing.

4. RESULTS

Figures 2–7 show the main results obtained numerically for the frictional melting of the long bearing. The liquid film thickness (Fig. 2) has a relatively sharp minimum near the leading line of the shaft (i.e. near $\beta = \pi/2$). The minimum migrates toward the exit from the relative motion gap as the applied force (f) increases. The converging–diverging shape of the liquid film in this frontal region is similar to the shape of the liquid film caused by frictional melting under a plane slider [19, 20]. As was anticipated during the formulation of the numerical method, the film thickness $\tilde{\delta}$ blows up at the entrance ($\beta = 0$) and the exit ($\beta = \pi$): the actual asymptotic expressions in the two limits are $\tilde{\delta} = 4/\tilde{V}\beta$ and, respectively, $\tilde{\delta} = 4/\tilde{V}(\pi - \beta)$.

Nondimensionalized as $\tilde{\delta}$, the film thickness is relatively insensitive to the angular speed parameter Ω. In view of the $\tilde{\delta}$ definition (16), this means that the actual film thickness (δ) decreases as the angular speed (ω, or U) increases.

Figure 3 shows two sets of results that go together, the negative of the pressure gradient ($\tilde{G}$) and the corresponding pressure distribution over the contact region ($\tilde{P}$). The pressure reaches a sharp peak in the vicinity of the line of minimum film thickness, and the peak migrates toward the exit end as the applied force increases. A region of negative pressures emerges in the vicinity of the exit if the applied force f becomes sufficiently small. Since the film analysis breaks down if cavitation occurs in this region, we limited the calculations of f values that are larger than about 0.25, so that the region of negative pressures is insignificant.

The tilt angle θ_0 is reported in Fig. 4, in which $\theta_0 = 90°$ would represent a rotating shaft that advances in the direction of the applied force. We see that θ_0 is less than 90° even as f becomes small, which means that the direction in which the shaft erodes the bearing is similar to the one shown in Fig. 1. The deviation from perfect alignment ($\theta_0 = 90°$) becomes more accentuated at large enough f values, and as the angular speed increases.

In Fig. 5 we see the speed with which the shaft advances into the bearing. The speed increases with the applied force. The effect of the angular speed on the melting speed is somewhat deceiving, because $\tilde{V}$ appears to be relatively insensitive to Ω. In fact, the physical melting speed V increases with the angular speed, as shown by the $\tilde{V}$ definition (16). The insensitivity of $\tilde{V}$ to Ω is a sign that the melting speed was scaled correctly in equation (16).

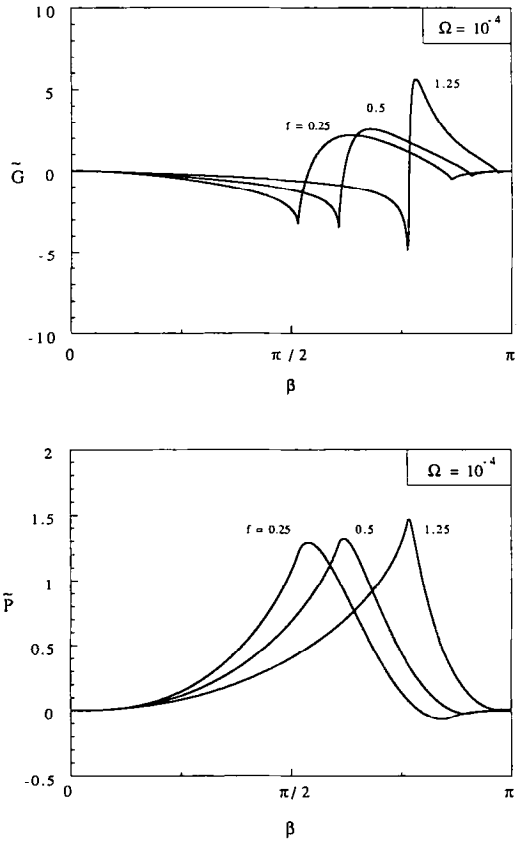

FIG. 3. The negative pressure gradient (top), and the corresponding pressure distribution along the circumference of contact (bottom), during the frictional melting of a long bearing.

A correlation for the $\tilde{V}(f,\Omega)$ results plotted in Fig. 5 can be developed by noting that $\tilde{V}$ appears to increase exponentially in f. Indeed, this relationship can be demonstrated analytically by first non-dimensionalizing equation (10), and taking the $d(\ )/df$ derivative of every term. Next, equation (18) can be integrated from $\beta = 0$ to $\beta = \pi$, and then

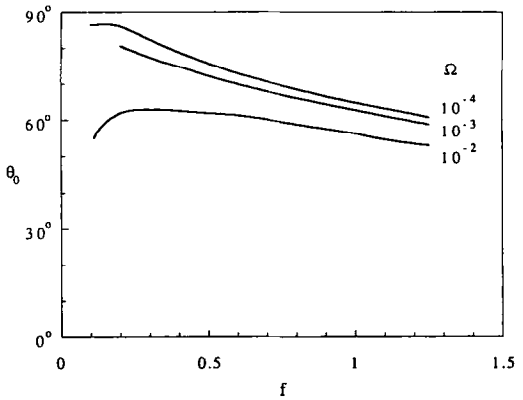

FIG. 4. The angle θ_0 defined in Fig. 1, for the direction of melting due to friction in a long bearing.

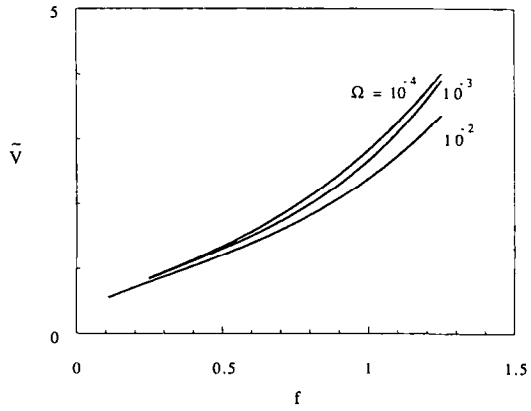

FIG. 5. The speed of advancement into a long bearing, during melting due to viscous dissipation in the liquid film.

differentiated twice with respect to f. Combined, these two steps lead to a second order differential equation with one unknown coefficient, and a solution of type $\tilde{V} = c_1 \exp(c_2 f)$. This expression reproduces within 0.1% the ($\Omega = 10^{-3}$, $f = 0.5$–1.5) data of Fig. 5 if $c_1 = 0.625$ and $c_2 = 1.456$.

The shear stress distribution over the shaft surface is shown in the upper half of Fig. 6. The local shear

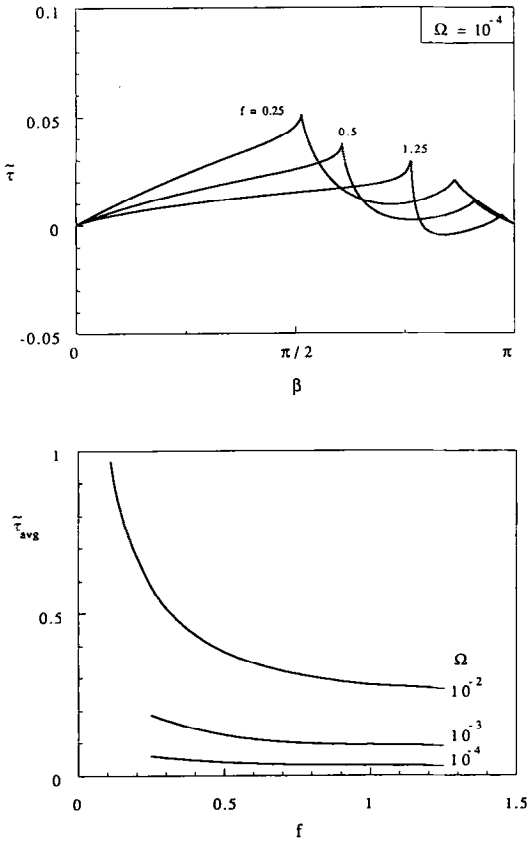

FIG. 6. The local (top) and average (bottom) shear stress experienced by the shaft during the frictional melting of a long bearing.

stress $\tilde{\tau}$ has two sharp peaks, a high one near the line of minimum film thickness, and a lower one near the exit, i.e. at the end of the region of nearly constant film thickness (Fig. 1). The effects of Ω and f are illustrated in the lower part of Fig. 6, where the ordinate shows the perimeter-averaged shear stress

$$\tilde{\tau}_{avg} = \frac{1}{\pi}\int_0^{\pi} \tilde{\tau}\, d\beta. \tag{41}$$

This integral was computed in the same way as the $\tilde{G}$ integral of equation (35). The frictional torque per unit axial length experienced by the shaft is equal to $\pi FR\tilde{\tau}_{avg}$. This quantity is proportional to the product $f \cdot \tilde{\tau}_{avg}$: it can be shown that this product increases as Ω and f increase. In conclusion, the torque increases as the angular speed and the applied force increase.

The upper part of Fig. 7 shows the temperature variation along the adiabatic surface of the shaft (T_s), relative to the bearing surface (T_m). The shaft surface may be modelled as adiabatic when the shaft length/diameter ratio is large, or when the shaft is a poorer thermal conductor than the phase-change material. It is easy to show that the nondimensional shaft surface temperature shown in the figure,

$$\tilde{T}_s = \frac{T_s - T_m}{\mu U^2/k} \tag{42}$$

can be deduced from the flow solution discussed already,

$$\tilde{T}_s = \frac{f^2}{24}\tilde{\delta}^4\tilde{G}^2 + \frac{1}{2} - \frac{f}{6}\tilde{\delta}^2\tilde{G}^2. \tag{43}$$

The shaft surface temperature is higher in the region situated upstream of the line of minimum film thickness, and increases as the applied force increases. The effect of f is shown more clearly in the lower part of Fig. 7, where $\tilde{T}_{s,avg}$ is the result of averaging $\tilde{T}_s$ over the perimeter of contact. The Ω effect is weak, however, this means only that the average temperature difference between the shaft and the bearing ($T_s - T_m$) scales as $\mu U^2/k$, or as the angular speed squared, as shown in equation (42).

By using equations (43) and (18), it can be shown that the shaft surface temperature can be expressed as a function of only $\tilde{\delta}(\beta)$ and β, namely, $\tilde{T}_s = (1/2)(\tilde{V}\tilde{\delta}\sin\beta - 1) - (\pm 3^{-1/2})(C\tilde{V}\tilde{\delta}\sin\beta - 1)^{1/2} + 1/2$, in which the $\pm$ sign corresponds to the sign of $\tilde{G}$. This expression shows that $\tilde{T}_s$ is small when $\tilde{\delta}$ is small. In particular, when $\tilde{V}$ is of order 1 (Fig. 5) and β in the vicinity of 140°, the above expression yields a $\tilde{T}_s$ value of order 0.5, which agrees with the results plotted numerically in Fig. 7 (top).

The shaft temperature distribution has the additional property that the entrance and exit temperatures are the same, $\tilde{T}_s \to 3$ for $\beta \to 0$ or $\beta \to \pi$, regardless of the values assigned to Ω and f. This $\tilde{T}_s$ limit can be proven analytically, and is a constant of the model. It means that the shaft surface temperature is continuous around the back side of the shaft, if that side continues to be modelled as adiabatic.

A related limit that can be derived analytically is $\tilde{\delta}^2\tilde{G} \to -6/f$ for $\beta \to 0$ or $\beta \to \pi$. This limit shows that near the exit ($\beta \lesssim \pi$) the pressure gradient must always be positive ($-\tilde{G} > 0$), or, since $\tilde{P}(\pi) = 0$, that the pressure in that region must be negative. Furthermore, since $-\tilde{G}$ is proportional to $1/f$ as $\beta \to \pi$, the magnitude (modulus) of $\tilde{P}$ decreases as f increases, and so does the β range occupied by the region of negative pressures. This behavior is confirmed by the numerical results seen already in Fig. 3 (bottom).

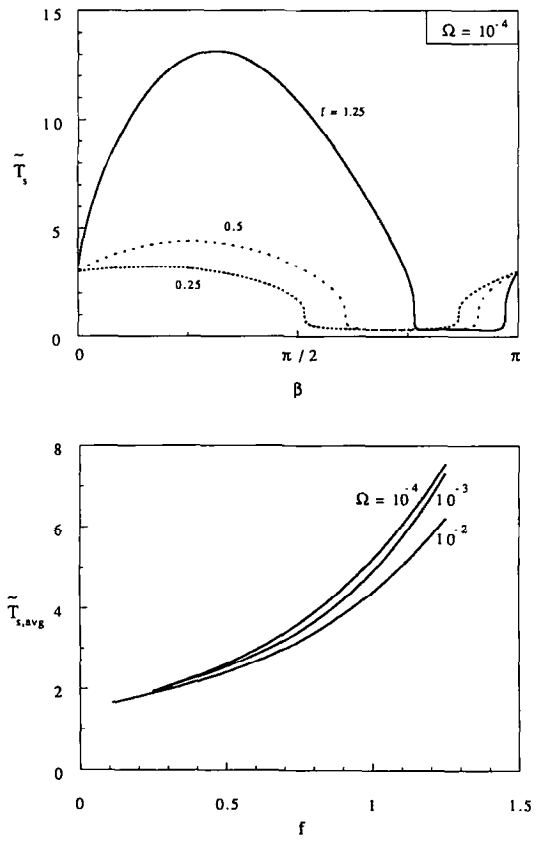

FIG. 7. The local (top) and average (bottom) temperature difference between the shaft and the bearing during the frictional melting of a long bearing.

5. THE SHORT BEARING ($B \ll R$): MELTING DUE TO VISCOUS DISSIPATION

In this section we turn our attention to an entirely different regime of the frictional melting phenomenon, namely, the erosion of a bearing with axial length B considerably smaller than the shaft radius (Fig. 8). This is the opposite of the geometric limit analyzed until now (Fig. 1). We begin with the assumption that the pressure is uniform (zero) everywhere outside the contact melting region. The following features can be expected in the limit $B/R \to 0$:

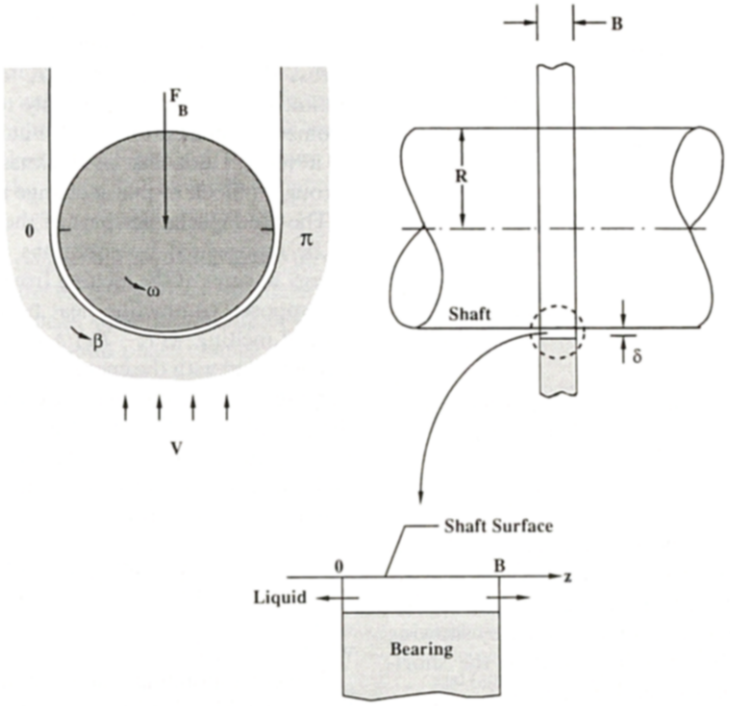

FIG. 8. The melting of a short bearing.

(a) The liquid will flow strictly in the axial direction z, regardless of the position β around the perimeter of contact (see Fig. 8 detail). In other words, in this limit the liquid flows in the direction perpendicular to the peripheral velocity of the shaft. This feature does not have to be demonstrated analytically here, because it was proven already in the study of the frictional melting of a narrow flat blade aligned with the direction of relative motion [20].

(b) A consequence of the z orientation of the squirting liquid is that the heat generation effect is due entirely to the β oriented Couette component of the flow. At any β, this heat generation rate is independent of z, and so is the film thickness, $\delta(\beta)$. The heat generation rate integrated across the film thickness is $\mu(U/\delta)^2\delta$.

(c) The pressure distribution that emerges after solving the appropriate thin-film lubrication problem is parabolic in z,

$$P(z,\beta) = \frac{6\mu V}{\delta^3} z(B-z). \tag{44}$$

This can be used to show that at any β the pressure averaged axially (from $z = 0$ to $z = B$) is

$$P_{avg}(\beta) = \frac{\mu V B^2}{\delta^3}. \tag{45}$$

(d) The shaft advances into the bearing in the direction of the applied force, or $\theta = 90°$. This is again due to the fact that the melt squirts in the positive and the negative z directions, and that the pressure is zero at $z = 0$ and $z = B$ for all values of β.

These features make it possible to obtain an analytical solution for the frictional melting process. The statement that the shaft surface is adiabatic, i.e. that the heat generation rate escapes entirely into the melting front, $\mu(U/\delta)^2\delta = \rho h_{sf} V \sin\beta$, yields

$$\delta = \frac{\mu U^2}{\rho h_{sf} V \sin\beta}. \tag{46}$$

This film thickness is symmetric about $\beta = \pi/2$. Equation (46) can be substituted in equation (45) to estimate the total force exerted by the shaft on the bearing,

$$F_B = \int_0^\pi P_{avg} B \sin\beta \, R \, d\beta = \frac{3\pi}{8} \mu R B^3 V^4 \left(\frac{\rho h_{sf}}{\mu U^2}\right)^3. \tag{47}$$

Equation (47) shows that the melting speed V increases as $F_B^{1/4}$, and as $U^{3/2}$, or $\omega^{3/2}$. It is worth comparing equation (47) with Fig. 5 and the $\tilde{V}$ definition (16), to see the fundamental difference between the scales of frictional melting in a short bearing and in a long bearing. By defining the average force per unit length $\bar{F} = F_B/B$ and its nondimensional counterpart cf. equation (22), namely $\bar{f} = \bar{F}/\rho h_{sf} R$, it is possible to rewrite equation (47) as

$$\tilde{V} = 0.960\left(\frac{R}{B}\right)^{1/2} \bar{f}^{1/4}. \tag{48}$$

Equation (48) agrees qualitatively with Fig. 5 (the f effect, and the insensitivity to Ω), except that the factor

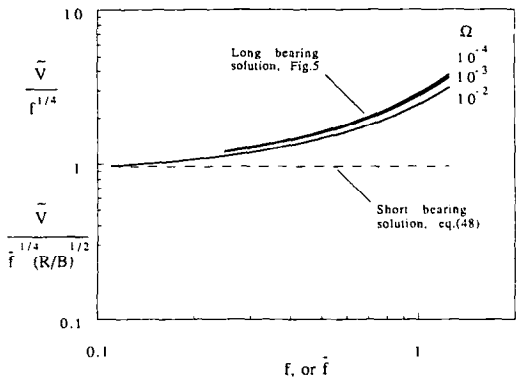

FIG. 9. Comparison between the frictional melting speeds through a long bearing and a short bearing.

$(R/B)^{1/2}$ is new. This new factor is greater than 1, therefore, equation (48) shows that the melting rate is considerably greater when the bearing is short. Figure 9 emphasizes this important difference by showing the long-bearing solution $\tilde{V}/f^{1/4}$ next to the short-bearing solution expressed as $\tilde{V}/\bar{f}^{1/4}(R/B)^{1/2}$.

As a numerical example, consider a copper bearing with $R = 1$ cm, $B = 0.2$ cm, $\omega = 3600$ r.p.m., and the total load $F_B = 240$ N. The properties of liquid copper at the melting point (1356 K) are $\rho = 8940$ kg m^{-3}, $h_{sf} = 134$ kJ kg^{-1}, and $\mu = 0.0044$ kg s^{-1} m^{-1}. In this case equation (47) yields $V \cong 0.1$ mm s^{-1}, which says that the shaft will erode the bearing to a depth of 1 mm in about 10 s. Equation (46) and $\beta = \pi/2$ can be used to show that δ is of the order of 1 μm. This means that the ratio δ/R is of order 10^{-4}, which validates the thin-film assumption made in the analysis. The film Reynolds number $\rho U\delta/\mu$ is of order 1, and the Peclet number $U\delta/\alpha$ is of order 10^{-3}. These orders of magnitude are consistent with the assumptions that liquid inertia is negligible in the momentum balance, and convection is a negligible effect in the energy balance.

6. THE SHORT BEARING: MELTING DUE TO IMPOSED TEMPERATURE DIFFERENCE

The flow features identified in the preceding section are an opportunity to extend to the class of short bearings the embedded cylinder contact melting problem analyzed earlier by Moallemi and Viskanta [15]. They had documented analytically and experimentally the contact melting around a hot cylinder embedded in a block of phase-change material. Their problem is similar to the long bearing configuration of Fig. 1, except that the heating is due to an imposed temperature difference $(T_s - T_m)$, instead of viscous dissipation in the melt.

Consider again the geometry of Fig. 8, in which the axial length of the region of contact melting (B) is considerably smaller than the cylinder radius. The cylinder temperature is fixed at some level (T_s) above the melting point (T_m). The shaft may be rotating, however, the viscous dissipation effect is negligible with respect to the conduction heat transfer imposed across the liquid film, from T_s to T_m. The solution outlined below applies not only to the short bearing geometry sketched in Fig. 8, but also to the sinking of a vertical hot disc of thickness B and radius R, through a block of phase-change material.

The fluid mechanics part of the solution continues to be represented by equations (44) and (45). The energy balance at the melting front, however, involves the imposed conduction heat transfer and the latent heat of melting, $k(T_s - T_m)/\delta = \rho h_{sf} V \sin\beta$. This can be compared with the energy balance that led to equation (46), to conclude that the only difference between the preceding section and this one is that the group μU^2 is replaced by $k(T_s - T_m)$ in the energy balance and the emerging results. In this way, in place of equation (47) we write

$$\bar{F}\left(\frac{R}{B}\right)^2 = \frac{3\pi}{8}\mu V^4\left[\frac{\rho h_{sf} R}{k(T_s - T_m)}\right]^3 \qquad (49)$$

where $\bar{F} = F_B/B$.

The corresponding result for the long bearing can be found in Moallemi and Viskanta [15], and rewritten as

$$F = \frac{16}{5}\mu V^4\left[\frac{\rho h_{sf} R}{k(T_s - T_m)}\right]^3 \qquad (50)$$

where F is the force applied per unit axial length. By comparing equations (49) and (50) we note that the order-of-magnitude difference between the results for the short bearing and the long bearing is attributed to the factor $(R/B)^2 \gg 1$. The speed of melting through the short bearing exceeds by a factor of order $(R/B)^{1/2}$ the speed of melting through the corresponding long bearing. This difference is analogous to what we found in Fig. 9 for the short and long bearings melting under the influence of viscous dissipation.

7. CONCLUDING REMARKS

In this paper we described three limiting regimes of the phenomenon of contact melting and lubrication around a rotating shaft embedded in a solid phase-change material. The limiting regimes are:

1. The long bearing with melting due to frictional heating in the melt layer. The global results for this regime are reported in Figs. 4–7. Noteworthy is the $90°-\theta_0$ angle between the applied force and the direction in which the shaft sinks into the bushing (Fig. 4), the relation between the sinking speed and the applied force (Fig. 5), and the relation between the applied force and the torque (Fig. 6, bottom).

2. The short bearing with melting due to frictional heating. In this limit the melt is ejected longitudinally, i.e. in the direction perpendicular to the peripheral velocity of the shaft (Fig. 8). The shaft migrates into the bushing in the same direction as the applied force,

and the relation between the speed of migration and the applied force is given in equation (47).

3. The short bearing, or short cylinder (disc), with melting due to an imposed temperature difference. The hot cylinder migrates into the solid in the same direction as the applied force. Equation (49) shows the relation between the speed of migration and the applied force.

Another way to review the progress made in this study is to consider the earlier work of Moallemi and Viskanta [15], which dealt with the sinking of a long cylinder into a block of solid phase change material. In their case the cylinder was heated to a prescribed temperature, and did not rotate. On this background, the present study shows that the contact melting phenomenon may depart from the limit documented by Moallemi and Viskanta [15] in three different respects:

(i) the axial length of contact may be shorter than the cylinder radius,
(ii) the cylinder may rotate inside the solid phase-change material, and
(iii) the melting may be caused by frictional heating, instead of an imposed temperature difference.

REFERENCES

1. J. Bishop and C. I. Ettles, The seizure of journal bearings by thermoelastic mechanism, *Wear* **79,** 37–52 (1982).
2. K. F. Dufrane and J. W. Kannel, Thermally induced seizures of journal bearings, *J. Tribology* **111,** 288–292 (1989).
3. M. M. Khonsari and H. J. Kim, On thermally induced seizure in journal bearings, *J. Tribology* **111,** 661–667 (1989).
4. D. Nicholas and Y. Bayazitoglu, Heat transfer and melting front within a horizontal cylinder, *ASME J. Solar Energy Engng* **102,** 229–232 (1980).
5. F. E. Moore and Y. Bayazitoglu, Melting within a spherical enclosure, *ASME J. Heat Transfer* **104,** 19–23 (1982).
6. M. Bareiss and H. Beer, An analytical solution of the heat transfer process during melting of an unfixed solid phase change material inside a horizontal tube, *Int. J. Heat Mass Transfer* **27,** 739–746 (1984).
7. A. Prasad and S. Sengupta, Numerical investigation of melting inside a horizontal cylinder including effects of natural convection, *ASME SED* **1,** 19–26 (1985).
8. A. Prasad and S. Sengupta, Numerical investigation of melting inside a horizontal cylinder including the effects of natural convection, *ASME J. Heat Transfer* **109,** 803–806 (1987).
9. A. Saito, Y. Utaka and Y. Tokihiro, On the contact heat transfer with melting (the melting on the inner surface of a horizontal cylindrical tube), *JSME International Journal* Ser. II, **31**(1), 58–65 (1988).
10. S. K. Roy and S. Sengupta, An analysis of the melting process within a spherical enclosure, *ASME SED* **1,** 27–32 (1985).
11. S. K. Roy and S. Sengupta, The melting process within spherical enclosures, *ASME J. Heat Transfer* **109,** 460–462 (1987).
12. P. A. Bahrami and T. G. Wang, Analysis of gravity and conduction-driven melting in a sphere, *ASME J. Heat Transfer* **109,** 806–809 (1987).
13. E. Said and S. Sengupta, Phase change heat transfer inside a horizontal tube: effects of Rayleigh number, ASME/NHTC Paper No. 84-HT-4, Buffalo, N.Y., Aug. (1984).
14. S. H. Emerman and D. L. Turcotte, Stokes's problem with melting, *Int. J. Heat Mass Transfer* **26,** 1625–1630 (1983).
15. M. K. Moallemi and R. Viskanta, Melting around a migrating heat source, *ASME J. Heat Transfer* **107,** 451–458 (1985).
16. M. K. Moallemi and R. Viskanta, Experiments on fluid flow induced by melting around a migrating heat source, *J. Fluid Mechanics* **157,** 35–51 (1985).
17. S. A. Fomin and S. Cheng, Optimization of the heating surface shape in the contact melting problem, Third International Conference on Inverse Design Concepts and Optimization in Engineering Sciences (ICIDES-III), Editor: G. S. Dulikravich, Washington, D.C., October 23–25 (1991).
18. M. K. Moallemi, B. W. Webb and R. Viskanta, An experimental and analytical study of close-contact melting, *J. Heat Transfer* **108,** 894–899 (1986).
19. G. P. Beretta, A. Niro and M. Silvestri, Solid slider bearings lubricated by their own melting or sublimation, *J. Tribology* **109,** 296–300 (1987).
20. A. Bejan, The fundamentals of sliding contact melting and friction, *ASME J. Heat Transfer* **111,** 13–20 (1989).
21. T. Hirata, Y. Makino and Y. Kaneko, Analysis of close-contact melting for octadecane and ice inside isothermally heated horizontal rectangular capsule, *Int. J. Heat Mass Transfer* **34,** 3097–3106 (1991).
22. B. W. Webb, M. K. Moallemi and R. Viskanta, Experiments on melting of unfixed ice in a horizontal cylindrical capsule, *ASME J. Heat Transfer* **109,** 454–459 (1987).
23. A. Saito, Y. Utaka, M. Akiyoshi and K. Katayama, On the contact heat transfer with melting (1st report: experimental study), *Bulletin of JSME* **28**(240), 1142–1149 (1985).
24. A. Saito, Y. Utaka, M. Akiyoshi and K. Katayama, On the contact heat transfer with melting (2nd report: analytical study), *Bulletin of JSME* **28**(242), 1703–1709 (1985).
25. S. Nagakubo and A. Saito, Numerical analysis on a direct contact melting process, *Transactions of the Japanese Society of Refrigeration* **4,** 37–45 (1987).
26. G. Golub and J. Welsch, Calculation of Gauss quadrature rules, *Math. Comp.* **26**(106), 221–231 (1969).
27. A. Stroud and D. Secrest, *Gaussian Quadrature Formulas*. Prentice-Hall, Englewood Cliffs, NJ (1966).